

Multipath Model and Exploitation in Through-the-Wall and Urban Radar Sensing

Pawan Setlur, Moeness Amin, and Fauzia Ahmad
Radar Imaging Lab, Center for Advanced Communications,
Villanova University, Villanova, PA 19085, USA.
E-mail: {pawan.setlur, moeness.amin, fauzia.ahmad}@villanova.edu

Abstract— We derive a multipath model for sensing through walls using radars. The model considers propagation through a front wall and specular reflections at interior walls in an enclosed room under surveillance. The model is derived such that additional eigenrays can be easily accommodated. A synthetic aperture radar (SAR) system is considered and stationary or slowly moving targets are assumed. The focused downrange and crossrange locations of multipath ghosts are established and validated using numerical as well as experimental data. The multipath model permits an implementation of a multipath exploitation algorithm, which associates as well as maps each target ghost back to its corresponding true target location. In doing so, the proposed algorithm improves the radar system performance by aiding in ameliorating the false positives in the original SAR image as well as increasing the signal to clutter ratio (SCR) at the target locations, culminating in enhanced behind the wall target detection and localization.

Keywords- Through-the-wall radar, multipath exploitation, eigenrays, least squares, SAR

I. INTRODUCTION

Through-the-wall (TTW) radar and urban sensing address the desire to obtain the electromagnetic (EM) blueprint and the layout of the building along with traditional radar capabilities, such as detection, localization, and classification of one or more targets inside rooms or buildings [1]. Much of the recent literature on urban sensing and TTW radar has focused on wall position estimation or the detection and localization of moving or stationary targets, but has not addressed the explicit problem of target multipath [1-5]. The existence of targets inside a room or an enclosed structure is deemed to introduce ghosts in the beamformed SAR images. These ghosts lie on or near the vicinity of the back and side walls, leading to a cluttered image with several false positives. Without a reasonable TTW multipath model, it becomes difficult to associate a ghost to a particular target.

Identifying the nature of the targets in the image and tagging the ghosts with their respective target according to a developed multipath model, although important to reduce false alarms, is not considered by itself and is not the final goal of a high TTW imaging system performance. Since each multipath provides some information about the target, it becomes prudent to utilize the multipath rather than ignore it, once identified. The utilization or exploitation of the multipath to our advantage represents a paradigm shift when compared to the classical approach of ignoring or mitigating it.

In this paper, we derive a multipath model, as well as provide a multipath exploitation technique which associates and then maps the multipath ghosts back to their true target locations. The multipath exploitation technique presented here is different from those techniques which exploit multipath in the absence of direct line of sight, as discussed, for example, in [6-9], and, moreover, it serves a different purpose. In the underlying problem, there is no issue of direct line

of sight, as all targets are obstructed by the front wall. Rather, we are interested in detecting the behind the wall targets and deducing their locations from the many ghosts in the image.

For through-the-wall radar imaging applications, existence of multipath has been recently demonstrated for stationary targets in [10-12] for TTW scenarios. In [10], the authors use distributed fusion to get rid of the false targets caused either from multipath or target interactions for stationary scenes after suitable image registration. In [11], time reversal techniques are used to alleviate ghosting and clutter from the target scene and in [12], a SAR image of a human inside a room is shown along with possible multipath ghosts. However, no more rigorous multipath modeling and analysis are presented in the aforementioned references [10-12] and the references therein.

There are three major contributions in this paper. First, we derive a model for the multipath in an enclosed room comprising four walls and illustrate the resulting multipath ghosts in the room. Second, we demonstrate analytically that the multipath as seen by each sensor is displaced, and, therefore, we derive the actual focusing positions of the ghosts in downrange and crossrange. Third, via our model, we exploit the multipath to associate as well as map the ghosts back to the true target location, thereby, alleviating the false positives and increasing the signal to clutter ratio (SCR) at the target location. It is noted that the proposed exploitation algorithm only maps back target-wall interactions; target-target interactions are left as is. The multipath exploitation algorithm is inspired by the work in [13]. The difference, however, is that we are not striving to reveal the shadowed regions of the target via its multipath, as in [13]. In our case, we deal with targets with arbitrary dielectric constants, and wish to associate and map each multipath to its true target location. The multipath model derived here is an extension to the model presented by us in [14-15], which considered moving targets using both Doppler only and range-Doppler radars, but

no SAR or multiple antennas imaging system was employed. Note that the analyses provided for stationary targets can be extended to moving targets in the context of a SAR-MTI system, but it is outside the scope of this paper. Although the multipath model presented deals with walls, reflections from the ceiling and floor can be handled readily, similar to the work in [16, ch. 6].

The paper is organized as follows. In Section II, fundamental equations, describing TTW beamforming, are presented. In Section III, we derive the multipath analytical model. In Section IV, the multipath exploitation algorithm is presented. Section V provides supporting simulation results based on numerical and experimental data, and conclusions are drawn in Section VI.

II. THROUGH-THE-WALL RADAR IMAGING: BACKGROUND

In this section, we describe the standard through-the-wall beamforming approach [17-22]. We consider a SAR system in which a single antenna at one location transmits and receives the radar return, and then moves to the next location and repeats the same operation along the axis parallel to the front wall [17]. Assume N monostatic antenna locations. The setup is as depicted in Fig. 1. Consider a point target at location $\mathbf{x}_t = [x_t, y_t]^T$. At each antenna position, the radar transmits a pulsed waveform $s(t)$, where ' t ' indexes the time within the pulse, and measures the reflected signal. The baseband target return at the n -th antenna position is given by,

$$r_n(t) = T_n^2(\mathbf{x}_t) a(\mathbf{x}_t) s(t - 2\tau_n(\mathbf{x}_t)) e^{-j2\omega_c \tau_n(\mathbf{x}_t)} \quad (1)$$

where $a(\mathbf{x}_t)$ represents the target reflectivity, ω_c represents the carrier frequency, $T_n(\mathbf{x}_t)$ is the complex amplitude associated with the one-way propagation through a dielectric wall for the n -th antenna location [23], and $\tau_n(\mathbf{x}_t)$ represents the one-way through-the-wall propagation delay from the n -th antenna location to the target. The scene of interest comprises several pixels indexed by the downrange and the crossrange. The complex composite return from the p -th pixel location \mathbf{x}_p

is obtained by applying time delays to the N received signals, followed by weighting and summing the results. That is,

$$r(t; \mathbf{x}_p) = \sum_{n=1}^N w_n r_n(t + 2\tau_n(\mathbf{x}_p)) e^{j2\omega_c \tau_n(\mathbf{x}_p)} \quad (2)$$

The signal $r(t; \mathbf{x}_p)$ is passed through a matched filter, with impulse response $h(t) = s^*(-t)$. The complex amplitude assumed by the pixel \mathbf{x}_p in the image $I(\cdot)$ is obtained by sampling the matched filter output at time $t=0$,

$$I(\mathbf{x}_p) = \{r(t; \mathbf{x}_p) * h(t)\} \big|_{t=0} \quad (3)$$

Equations (2-3) describe the standard beamforming approach in TTW radar imaging. It is noted that if the imaged pixel is in the vicinity of or at the true target location, then the complex amplitude in (3) assumes a high value as given by the system's point spread function. The process described in (2) and (3) is carried out for all pixels in the scene of interest to generate the image of the scene.

The beamforming approach as described above is pertinent to a point target in a two-dimensional (2D) scene. Extensions to three-dimensional (3D) scenes and spatially extended targets are discussed in [16, 21]. It is noted that, in the above beamforming description, we have not considered the multipath returns; neither have we addressed the specificities of calculating the delays, $\tau_n(\cdot)$, and the complex amplitudes, $\Gamma_n(\cdot)$, all of which will be treated in details in the next section. In the rest of the paper, we will assume that the weights $w_n = 1, \forall n$ and the target has unit reflectivity.

III. MULTIPATH MODEL

Consider a room under surveillance using a SAR system. A priori knowledge of the room layout, i.e., wall locations and material properties, is assumed. The scene of observation relative to the n -th sensor location is as shown in Fig. 2. The origin is marked as point ‘O’ in the figure, and the standard convention for the positive x- and y- axes is assumed. The front wall has a thickness and dielectric constant given as d_1 and ε_1 , respectively. For simplicity of notation, we assume that the back and the side walls have ε_1 as their dielectric constants. The side walls, labeled as wall-1 and wall-3, have a length denoted as D_1 , whereas the front wall and the back wall (wall-2) have a length denoted as D_2 . The n -th sensor location is given by $\mathbf{R}_n = [-D_{xn}, 0]^T$. The target is stationary and at position $\mathbf{A} = [-x_t, y_t]^T$. The standoff distance from the front wall is constant for each sensor position constituting the synthetic aperture, and is denoted as D_y . In the figure, we consider the direct path, referred to as path-A, and three additional paths, namely, paths-B, C, and D, which correspond to single-bounce multipath. In general, there exist other paths which can contribute to the multipath returns; these include multiple bounces from the back and side walls as well as paths that include multiple reflections within each of the four walls themselves. Examples of the former and the latter are provided in Fig. 3. Such paths are defined as higher-order multipaths. Hence, in Fig. 2, we have considered only first-order multipaths. It is noted that higher-order multipaths are weaker compared to the first-order multipaths due to the secondary reflections and refractions at the air-wall interfaces and high attenuation in the wall material. Therefore, we choose to exclude these paths from our model.

The walls are assumed smooth with specular reflections. The smoothness assumption is valid, since for TTW radars, the wavelength is much larger than the roughness of walls. Specular

reflections are a direct consequence of the wall smoothness, and necessitate that the angle of incidence be equal to the angle of reflection. Note that, in general, the back and side walls may each be of a different material (interior or exterior grade), and thus may assume different values of d and ε . If interior reflections inside these walls are considered, then the thickness of these walls are required, see for example [14-16]. However, since we have ignored such higher-order paths, we only require the dielectric constant of the back and side walls to be known. As the EM wave propagates through the front wall, it bends at the medium discontinuity as dictated by Snell's law, i.e., each of the paths, as seen in Fig. 2, has an associated angle of incidence and an angle of refraction. For example, the angles of incidence and refraction for path-B are denoted as $\psi_{iB}^{(n)}$ and $\psi_{rB}^{(n)}$, respectively. Similar nomenclature follows for the remaining paths.

Let the reflection points on wall-1, 2, and 3 be denoted by B_n , C_n , and D_n , with respective position vectors $\mathbf{B}_n = [y_{Bn}, 0]^T$, $\mathbf{C}_n = [x_{Cn}, D_1 + D_y]^T$, and $\mathbf{D}_n = [-D_2, y_{Dn}]^T$. It is clear that these positions are sensor position dependent. The one-way path delays for the four paths with the antenna at the n -th position, are denoted as $\tau_p^{(n)}$, $p \in \{A, B, C, D\}$, and can be readily derived as shown in Appendix-A. We can, therefore, write the signal returns as a superposition of the direct path and the multipath returns. For the n -th sensor position, we obtain

$$r_n(t) = \sum_{p \in \{A, B, C, D\}} T_{pn}^2 s(t - 2\tau_p^{(n)}) + \sum_{(p, q) \in \{A, B, C, D\}, p \neq q} T_{pn} T_{qn} s(t - \tau_p^{(n)} - \tau_q^{(n)}) \quad (4)$$

where T_{pn} is the complex amplitude associated with reflection and transmission coefficients for the one-way propagation along path- p . The expressions for T_{pn} are derived in the Appendix-B and depend on the angles of incidence, the angles of refraction, and dielectric properties of the walls. In (4), the first summation captures the two-way returns along the direct path and each

multipath. Specifically, the signal propagates along a particular path- p , $p \in \{A, B, C, D\}$, reaches the target and retraces the same path back to the radar, i.e., path- p . The multipath returns due to the combination paths are captured by the second summation, i.e., the wave initially travels to the target via path- p and returns to the radar through a different path- q , $q \in \{A, B, C, D\}$. The combination paths, therefore, imply a diffuse scatterer. From the analysis in Appendix-A, we can observe that the coordinates of the reflections at the back and side walls are sensor dependent, implying that the multipath presents itself at different locations to the different sensors. Location of the multipath as seen by each sensor and the actual focusing position of the resulting ghost are discussed next.

A. Location of Multipath Ghosts

Consider Fig. 2 and the combination path comprising of path-A and path-B, i.e., the ray travels to the target via path-A, and follows path-B back to the radar or vice versa. The point of reflection at wall-1 is sensor dependent, and, hence, denoted as B_n . The goal is to find the location of the multipath corresponding to the above combination path as seen by each of the N sensors.

For simplicity of analysis, consider the scenario with no front wall and only wall-1. The aim is to locate the multipath ghost as seen by the n -th sensor, i.e., $P_n^{w_1}$ represented by the vector $[-x_{pn}^{w_1}, y_{pn}^{w_1}]^T$. The superscript w_1 stresses that the ghost is associated with the reflection at wall-1. Consider the virtual target denoted as point A^1 , and whose coordinates are given by $[x_t, y_t]^T$, such that the distance $AB_n = A^1B_n$, which implies that

$$AR_n + AB_n + B_nR_n = AR_n + A^1R_n \quad (5)$$

Hence, the path length for the combination comprising of path-A and path-B is equal to the path length comprising of path-A, and the distance between the n -th sensor and the virtual target at A^1 .

To the n -th sensor, this path length appears as the traditional two way path length, $2R_n P_n^{w_1}$.

Therefore, we have

$$R_n P_n^{w_1} = \frac{AR_n + A^1 R_n}{2} \quad (6)$$

Consider Fig. 4, where we have introduced the virtual radar located on the other side of the wall. From geometry, it is readily seen that we now have a bistatic configuration with regard to the multipath. The multipath bistatic range is given by,

$$R_n A + R_n A^1 = R_n A^1 + R_n^1 A^1 \quad (7)$$

In the bistatic case, the multipath has an elliptical locus, whereas in the monostatic scenario it follows a circular locus. Since the multipath ghost is the same for both configurations, it is clear that the location of the ghost is at the intersection of the bistatic elliptical, and the monostatic circular loci. The equations for the ellipse and circle are readily given by,

$$\begin{aligned} \frac{x_{pn}^{w_1 2}}{(R_n P_n^{w_1})^2} + \frac{y_{pn}^{w_1 2}}{(R_n P_n^{w_1})^2 - D_{xn}^2} &= 1 \\ (x_{pn}^{w_1} + D_{xn})^2 + y_{pn}^{w_1 2} &= (R_n P_n^{w_1})^2 \end{aligned} \quad (8)$$

Solving (8) for a common intersection point we can readily see that $x_{pn}^{w_1} = 0$ is the only solution.

In other words, regardless of the location of the target its multipath always falls on the wall. The y-coordinate of $P_n^{w_1}$ can then be readily derived as

$$y_{pn}^{w_1} = \pm \sqrt{\frac{(AR_n + A^1 R_n)^2}{4} - D_{xn}^2} \quad (9)$$

In (9), the positive y-coordinate is considered as the other solution lies behind the radar. It is clear from (9) that the multipath ghost location is sensor dependent. Therefore, the locations of the target ghosts corresponding to the various sensor positions will be displaced from one another.

In the presence of the front wall, the solution is unchanged and trivially, the equations for the ellipse and circle are different than that presented in (8). Hence, for the scenario comprising of the front-wall and wall-1, the ghost appears on wall-1, and at the corresponding y-coordinate, $y_{pn}^{w_1}$, given by

$$y_{pn}^{w_1} = \left(\frac{(c\tau_A^{(n)} + c\tau_B^{(n)})}{2} + d_1(\sec(\psi_{ip}^{n(w_1)}) - \sqrt{\varepsilon_1} \sec(\psi_{rp}^{n(w_1)})) \right) \times \cos(\psi_{rp}^{n(w_1)}) \quad (10)$$

where $\psi_{ip}^{n(w_1)}$ and $\psi_{rp}^{n(w_1)}$ are, respectively, the angles of incidence and refraction for the ghost.

The solution in (10) depends on the angle $\psi_{ip}^{n(w_1)}$, which can be obtained by solving

$$d_1 \tan(\psi_{rp}^{n(w_1)}) + \left(\frac{(c\tau_A^{(n)} + c\tau_B^{(n)})}{2} - d_1 \sqrt{\varepsilon_1} \sec(\psi_{rp}^{n(w_1)}) \right) \sin(\psi_{ip}^{n(w_1)}) - D_x = 0 \quad (11)$$

So far, we have considered the ghost corresponding to wall-1; there exist two other ghosts tagged to the remaining walls, namely, wall-2, and wall-3. We can readily show, using similar analysis, that the ghost associated with wall-2 appears on wall-2, i.e., $y_{pn}^{w_2} = D_y + D_1$ at an x-coordinate given by

$$x_{pn}^{w_2} = -\sin(\psi_{ip}^{n(w_2)}) \times \left(d_1(\sqrt{\varepsilon_1} \sec(\psi_{rp}^{n(w_2)}) - \tan(\psi_{rp}^{n(w_2)}) \operatorname{cosec}(\psi_{ip}^{n(w_2)})) + D_x \operatorname{cosec}(\psi_{ip}^{n(w_2)}) - \frac{c\tau_A^{(n)} + c\tau_C^{(n)}}{2} \right) \quad (12)$$

The angles in the above equation are given by solving the equation,

$$d_y \sec(\psi_{ip}^{n(w_2)}) + (D_1 - d_1) \sec(\psi_{ip}^{n(w_2)}) + d_1 \sqrt{\varepsilon_1} \sec(\psi_{rp}^{n(w_2)}) - \frac{c\tau_A^{(n)} + c\tau_C^{(n)}}{2} = 0 \quad (13)$$

Likewise, the ghost associated with wall-3 appears at wall-3, i.e., $x_{pn}^{w_2} = -D_2$ and at a y-coordinate given by,

$$y_{pn}^{w_3} = \left(\frac{(c\tau_A^{(n)} + c\tau_D^{(n)})}{2} + d_1(\sec(\psi_{ip}^{n(w_3)}) - \sqrt{\varepsilon_1} \sec(\psi_{rp}^{n(w_3)})) \right) \cos(\psi_{rp}^{n(w_3)}) \quad (14)$$

The respective angles can be obtained by solving,

$$d_1 \tan(\psi_{rp}^{n(w_3)}) + \left(\frac{(c\tau_A^{(n)} + c\tau_D^{(n)})}{2} - d_1 \sqrt{\varepsilon_1} \sec(\psi_{rp}^{n(w_3)}) \right) \sin(\psi_{rp}^{n(w_3)}) - D_2 + D_x = 0 \quad (15)$$

From the above equations, it is again observed that the N sensors view the multipath ghosts, resulting from the combination paths associated with a particular wall, at different locations on that wall. That is, the multipath maybe regarded as a moving target. As a result, during beamforming, the multipath ghost appears at a different pixel in the vicinity of the true multipath locations. We note that the virtual target corresponds to two-way propagation along the single-bounce multipath, and is readily seen to lie outside the room perimeter. The multipath focusing pixel analysis for the combination paths is discussed next.

B. Multipath Focusing Analysis

Consider Fig. 5, which shows the multipath locations w.r.t to walls-1-3, and the focusing pixels w.r.t to these walls. Consider the multipath locations associated with wall-1; further assume that the focused multipath ghost appears at a pixel location given by

$$\mathbf{x}_p^{w_1} = [-\Delta x_1 + x_{p1}^{w_1}, \Delta y_1 + y_{p1}^{w_1}]^T \quad (16)$$

where $\mathbf{x}_{p1}^{w_1} = [x_{p1}^{w_1}, y_{p1}^{w_1}]^T$ is the true multipath location corresponding to the first sensor position.

Then, using a first order Taylor series expansion, which is valid under conditions of a small aperture [22] and when the focused ghost is in the vicinity of the true multipath locations, we obtain the difference in propagation delay between the focused multipath and the true multipath w.r.t the first sensor position as

$$\begin{aligned} \Delta \tau_1^{w_1} = & \Delta x_1 \frac{D_{x1} - D_y \tan(\psi_{ip}^{1(w_1)}) - d_1 \tan(\psi_{rp}^{1(w_1)}) - x_{p1}^{w_1}}{\sqrt{(D_{x1} - D_y \tan(\psi_{ip}^{1(w_1)}) - d_1 \tan(\psi_{rp}^{1(w_1)}) - x_{p1}^{w_1})^2 + (y_{p1}^{w_1} - D_y - d_1)^2}} \\ & + \Delta y_1 \frac{y_{p1}^{w_1} - D_y - d_1}{\sqrt{(D_{x1} - D_y \tan(\psi_{ip}^{1(w_1)}) - d_1 \tan(\psi_{rp}^{1(w_1)}) - x_{p1}^{w_1})^2 + (y_{p1}^{w_1} - D_y - d_1)^2}} \end{aligned} \quad (17)$$

Following the analysis in [22], (17) can be expressed as

$$\Delta \tau_1^{w_1} = \Delta x_1 \sin(\psi_{ip}^{1(w_1)}) + \Delta y_1 \cos(\psi_{ip}^{1(w_1)}) \quad (18)$$

In general, for the n -th sensor, we have

$$\Delta \tau_n^{w_1} = \Delta x_1 \sin(\psi_{ip}^{n(w_1)}) + (\Delta y_1 - (y_{pn}^{w_1} - y_{p1}^{w_1})) \cos(\psi_{ip}^{n(w_1)}), \quad n = 1, \dots, N \quad (19)$$

For the multipath to focus at the location $\mathbf{x}_p^{w_1}$, we must have,

$$\Delta \tau_n^{w_1} = 0, \quad \forall n = 1, \dots, N \quad (20)$$

This yields a least squares (LS) formulation, given by

$$\begin{aligned} \mathbf{A}_1 \mathbf{e}_1 &= \mathbf{b}_1, \quad \mathbf{e}_1 = [\Delta x_1, \Delta y_1]^T \\ \mathbf{A}_1 &:= [\mathbf{a}_1^{w_1} \quad \mathbf{a}_2^{w_1}]^T, \quad \mathbf{a}_1^{w_1} = [\sin(\psi_{p1}^{w_1}), \dots, \sin(\psi_{pN}^{w_1})]^T, \quad \mathbf{a}_2^{w_1} = [\cos(\psi_{p1}^{w_1}), \dots, \cos(\psi_{pN}^{w_1})]^T \\ \mathbf{b}_1 &:= [0, y_{p2}^{w_1} - y_{p1}^{w_1}, \dots, y_{pN}^{w_1} - y_{pN-1}^{w_1}]^T \odot \mathbf{a}_2^{w_1} \end{aligned} \quad (21)$$

where ' \odot ' denotes the Hadamard or element-wise product. The solution of (21) is readily obtained by $(\mathbf{A}_1^T \mathbf{A}_1)^{-1} \mathbf{b}_1$. As a special case, if the displacement between the multipath locations on wall-1 is uniform, i.e., $(y_{pn}^{w_1} - y_{p(n-1)}^{w_1}) = v_1 \approx \text{constant}$, then (19) can be rewritten as

$$\Delta \tau_n^{w_1} = \Delta x_1 \sin(\psi_{ip}^{n(w_1)}) + (\Delta y_1 - (n-1)v_1) \cos(\psi_{ip}^{n(w_1)}), \quad n = 1, \dots, N \quad (22)$$

A LS solution could then be formulated in a straightforward manner. Now considering the multipath w.r.t wall-2, we have the following LS formulation for the focused ghost pixel.

$$\begin{aligned} \mathbf{A}_2 \mathbf{e}_2 &= \mathbf{b}_2, \quad \mathbf{e}_2 = [\Delta x_2, \Delta y_2]^T \\ \mathbf{A}_2 &:= [\mathbf{a}_1^{w_2} \quad \mathbf{a}_2^{w_2}]^T, \quad \mathbf{a}_1^{w_2} = [\sin(\psi_{p1}^{w_2}), \dots, \sin(\psi_{pN}^{w_2})]^T, \quad \mathbf{a}_2^{w_2} = [\cos(\psi_{p1}^{w_2}), \dots, \cos(\psi_{pN}^{w_2})]^T \\ \mathbf{b}_2 &:= -[0, y_{p2}^{w_2} - y_{p1}^{w_2}, \dots, y_{pN}^{w_2} - y_{p1}^{w_2}]^T \odot \mathbf{a}_1^{w_2} \end{aligned} \quad (23)$$

Similarly, for the multipath from wall-3, we have

$$\begin{aligned} \mathbf{A}_3 \mathbf{e}_3 &= \mathbf{b}_3, \quad \mathbf{e}_3 = [\Delta x_3, \Delta y_3]^T \\ \mathbf{A}_3 &:= [-\mathbf{a}_1^{w_3} \quad \mathbf{a}_2^{w_3}]^T, \quad \mathbf{a}_1^{w_3} = [\sin(\psi_{p1}^{w_3}), \dots, \sin(\psi_{pN}^{w_3})]^T, \quad \mathbf{a}_2^{w_3} = [\cos(\psi_{p1}^{w_3}), \dots, \cos(\psi_{pN}^{w_3})]^T \\ \mathbf{b}_3 &:= [0, y_{p2}^{w_3} - y_{p1}^{w_3}, \dots, y_{pN}^{w_3} - y_{p1}^{w_3}]^T \odot \mathbf{a}_2^{w_3} \end{aligned} \quad (24)$$

The formulations in (21) and (23-24) assume that the sensor position increases from left to right. In other words, sensor-1 is at the left whereas sensor- N is at the right. When the multipath displacements are constant for wall-2 and wall-3, special cases of the LS can be derived as suggested in case of wall-1.

A preliminary simulation of the beamformed image of a single-target scene is shown, along with the back and side walls, in Fig. 6. The target is located at $(-4, 14)$ m. The front wall is not shown as the imaging dimensions exceed its downrange. The wall thickness and the dielectric constant are 0.2 m and 7.6, respectively. In this simulation, we did not include any multipath return associated with interior wall-3. However, we did include higher-order multipaths resulting from double-bounce between wall-1 and wall-2. Hence, the figure shows the true target and the strong multipath ghosts from first-order reflections at wall-1 and wall-2 as well as low magnitude ghosts corresponding to the higher-order multipaths. We observe that only the ghosts associated with first-order multipaths lie inside the room and are comparable in power to the returns from the target. On the other hand, the ghosts due to higher order multipaths as well as the virtual targets corresponding to two-way propagation along single-bounce multipaths are outside the enclosed structure. Furthermore, the higher-order multipath ghosts are of much lower power than the target and the first-order multipath ghosts. This validates our choice of restricting the analysis to first-order multipath ghosts, noting however that the model is capable of incorporating the higher-order multipaths.

IV. MULTIPATH EXPLOITATION

Noting that the multipath ghosts exist due to the presence of the target, we state our objective as follows. Given the beamformed image, $I(\cdot)$, our aim is to tag the multipath ghosts with the associated target via the model developed in Section III. The principle is captured in Fig. 7, which consists of two targets and six false positives or multipath ghosts. We desire to associate and map these ghosts to their respective true target locations. The main advantages of such an association or mapping are reduction in false positives in the original beamformed image, and an increase in the SCR at the true target coordinates. Note that the first advantage is directly implied in Fig. 7, whereas the second advantage is explained as follows.

For ease of exposition, the technique is explained considering the focused multipath ghost from wall-1. The technique for exploiting all the ghosts w.r.t to all three walls is enumerated subsequently. Let the complex amplitude of the pixel at (x, y) in the original beamformed image be denoted as $I(x, y), x \in X, y \in Y$. Here, X and Y index the crossrange and downrange, respectively. The image $I(\cdot)$ in practice consists of $N_x \times N_y$ pixels, representing the dimensions of the regions X and Y , respectively. Consider an arbitrary location indexed by $x_1 \in X, y_1 \in Y$, whose focused multipath ghost w.r.t wall-1 presents itself at location $[x_1^{w_1}, y_1^{w_1}]$, $x_1^{w_1} \in X, y_1^{w_1} \in Y$. Consider an intermediate image, wherein the association and mapping of the focused multipath ghosts is performed using simple 2D weighting functions. That is,

$$\begin{aligned}
 I_1(x_1, y_1) &\in \mathbb{C}^{N_x \times N_y} = \sum_{x_0 \in X} \sum_{y_0 \in Y} I(x, y) \Phi_1(\mathbf{x}_1^{w_1}, \mathbf{x}, \sigma^2) \Phi_2(\mathbf{x}_1, \mathbf{x}, \sigma^2) \\
 \mathbf{x} &:= [x, y]^T, \mathbf{x}_1 := [x_1, y_1]^T, \mathbf{x}_1^{w_1} := [x_1^{w_1}, y_1^{w_1}]^T \\
 \Phi_1(\mathbf{x}_1^{w_1}, \mathbf{x}, \sigma^2) &:= \exp\left(-\|\mathbf{x}_1^{w_1} - \mathbf{x}\|^2 / \sigma^2\right), \Phi_2(\mathbf{x}_1, \mathbf{x}, \sigma^2) := 1 - \exp\left(-\|\mathbf{x}_1 - \mathbf{x}\|^2 / \sigma^2\right)
 \end{aligned} \tag{25}$$

where $\Phi_1(\cdot)$ and $\Phi_2(\cdot)$ are the weighting functions and σ^2 is an arbitrary variance, which can assume different values, as will be seen in the simulations section. It is noted that in (25), these weighting functions are related to the two dimensional real Gaussian distributions. One can use weighting functions related to different symmetric distributions, such as the 2D Laplacian instead. However, the use of such other symmetric weighting functions is not pursued here. The role of $\Phi_1(\cdot)$ and $\Phi_2(\cdot)$ is explained as follows. Consider the weighting function $\Phi_1(\cdot)$; if the pixel \mathbf{x} is in the vicinity of the focused multipath ghost pixel $\mathbf{x}_1^{w_1}$ associated with the target location \mathbf{x}_1 , then $\Phi_1(\cdot)$ assumes a large weight. On the other hand, if \mathbf{x} is not in the vicinity of $\mathbf{x}_1^{w_1}$ then $\Phi_1(\cdot)$ assumes a low weight. The vicinity is obviously controlled by the variance parameter, σ^2 . Since an exponential function is used, the weights are always between 0 and 1, the lower bound being theoretically unachievable.

The weighting function, $\Phi_2(\cdot)$, serves two purposes. First, it rejects pixel locations in the vicinity of the imaged pixel, i.e., the location corresponding to the true target location $\mathbf{x} = \mathbf{x}_1$. As we have seen that although the focus point is singular, but due to the system's point spread function, some of the energy is spread to the neighboring pixels. To elaborate the second purpose, assume that the imaged pixel was located at $\mathbf{x}_1 = \mathbf{x}_1^{w_1}$, in which case we note that $I(x_1^{w_1}, y_1^{w_1})$ assumes a high value, since it is located at the focused multipath ghost. The weighting $\Phi_2(\cdot)$, in this case, serves to mitigate the contribution of the multipath pixels which will be in close proximity to the true target if it were at $\mathbf{x}_1^{w_1}$. In other words, as $\mathbf{x}_1^{w_1}$ is in the vicinity of wall-1 as demonstrated in Section II, and likewise, its associated multipath focused ghost, say $\mathbf{x}_m^{w_1}$, also appears in the vicinity of wall-1, and hence in the vicinity of $\mathbf{x}_1^{w_1}$. In such a scenario, the

weighting function $\Phi_1(\cdot)$ fails to serve its purpose and assumes a reasonable weight, whereas $\Phi_2(\cdot)$ assumes a low weight. Multiplication of these weighting functions yields an even smaller weight, thereby mitigating the contribution of the multipath pixels, as well as the point spread function at or in the vicinity of the imaged pixel $\mathbf{x}_1^{w_1}$. Consider Fig. 8, which shows three imaging locations at the multipath ghosts, and the mapping of the overlapping hypothesized ghosts back to these imaging locations. The weighting function $\Phi_2(\cdot)$ prevents such a mapping. In essence, the main contribution of $\Phi_2(\cdot)$ is to disallow energy to be focused back to the multipath ghost locations.

From our extensive simulations, we found that as the original image $I(\bullet)$ is complex-valued, summing or integrating across the multipath pixels may result in destructive interference yielding a poor SCR. An example of such a scenario is given in Section V. This loss of SCR is against our principle of multipath exploitation. To alleviate this problem, we use the intensity of the original beamformed image in (25) as

$$I_1(x_1, y_1) = \sum_{x \in X} \sum_{y \in Y} \|I(x, y)\|^2 \Phi_1(\mathbf{x}_1^{w_1}, \mathbf{x}, \sigma^2) \Phi_2(\mathbf{x}_1, \mathbf{x}, \sigma^2) \quad (26)$$

which implies an incoherent summation. Now considering the ghosts w.r.t the three walls, we can readily see that (26) is modified as

$$I_1(x_1, y_1) = \sum_{w_i=w_1}^{w_3} \sum_{x \in X} \sum_{y \in Y} \|I(x, y)\|^2 \Phi_1(\mathbf{x}_1^{w_i}, \mathbf{x}, \sigma^2) \Phi_2(\mathbf{x}_1, \mathbf{x}, \sigma^2) \quad (27)$$

Image $I_1(\bullet)$ will have no intensity at and near the vicinity of the focused multipath pixels. Hence, consider the following composite image obtained by simple pixel-wise multiplication.

$$I_f(x_1, y_1) = I_1(x_1, y_1) \times |I(x_1, y_1)| \quad (28)$$

The effect of pixel-wise multiplication in (28) is as follows. The image $I_1(\bullet)$ will have deep nulls at the hypothesized ghosts locations, whereas a large peak at the true target location. Thus, (28) is essentially a masking operation, nulling the ghosts in the original image $I(\bullet)$, and simultaneously enhancing the energy at the true target location. Hence, the composite image $I_f(\bullet)$ will alleviate the false positives, i.e., the multipath ghosts and increase the intensity of the true target pixel. In the approach described, the multipath ghost locations are readily obtained using the multipath focusing analysis in Section III. It is noted that, in practice, different targets may exhibit significantly weaker bistatic radar cross sections (RCS) relative to their monostatic RCS. Accordingly, some or maybe all of the target ghosts may go unnoticed. In this case, the proposed multipath exploitation approach will not prove beneficial as there may not be any increase in the target SCR.

Consider a scenario where one target presents itself at one of the other target's focused multipath ghost. Since multipath is unexploited in the original beamformed image, we would declare the presence of the target at the pixel in question. On the other hand, the proposed approach will map this target and of course the collocated multipath ghost back to the other target's location causing the second target to go undetected. The question then arises whether one should ignore the multipath ghosts and consider them as true targets or instead exploit the multipath ghosts. The former has an unreasonably high false alarm rate, whereas the latter yields poor target detection for the considered scenario, which, although rare, can occur in practice. However, noting that indoor targets of interest are typically in motion, it is reasonable to assume that a genuine target would not persist on a multipath ghost throughout the surveillance period. Hence, multipath exploitation should be preferred.

V. SIMULATIONS AND EXPERIMENTAL RESULTS

Certain parameters assume constant values throughout the simulations, unless explicitly mentioned. The length and width of the room are given by $D_i = 20$ m, $i = 1, 2$. The system operates at a carrier frequency of 1.8 GHz, with bandwidth of 400 MHz. There are 12 antenna locations starting at coordinates $(-10, 0)$ m, and are placed $\lambda / 4$ m apart to prevent spatial aliasing. The standoff distance $D_y = 4$ m and the 0.2 m thick front wall has a dielectric constant of 7.6, which is typical of concrete. The other three walls have similar dielectric properties. The dimensions and locations of the target and ghosts are in meters, unless mentioned otherwise. The image intensities are depicted in a dB scale, unless noted otherwise.

Consider the scenario in Fig. 6. Including the multipaths from wall-3, ignoring the higher-order multipaths, and setting the imaging dimensions to be approximately equal to the room dimensions, we obtain Fig. 9. The multipath ghosts from the three walls are clearly observed and appear well focused. These ghosts along with the true target show a spread in downrange and crossrange, which are attributed to the system point spread function. This spread was also seen in Fig. 6 but appeared to be smaller, since the imaging dimensions were much larger than the room dimensions. The ghosts w.r.t wall-2 and wall-3 in particular are focused at locations away from their respective walls. Table I provides the errors in the x and y coordinates of the actual ghost, and the predicted LS coordinates. Due to the point spread function, these errors are calculated as the magnitude difference between the coordinates of the maximum peak location of the ghost and the coordinates as predicted by the LS technique. Referring to the first row in the Table. I, we see that the locations as predicted by the LS are in error, the highest being w.r.t wall-3. The LS technique to estimate the locations of the focused multipaths are approximate as only a first order Taylor series is used, which are valid for small apertures and when the actual focusing pixel is

near the vicinity of the multipath locations (see also [22]). This approximation explains the error in the actual and estimated focused locations of the ghosts. In most cases, the errors are small. Employing higher-order Taylor series expansions may alleviate this error but at the expense of using sophisticated numerical solvers, and at a higher computational cost.

The images corresponding to Fig. 9 after multipath exploitation are presented in Fig. 10 and Fig. 11. The former utilizes a variance equal to the systems range resolution, whereas the latter uses a variance equal to the systems wavelength. When compared to Fig. 9, it is readily seen that the target is well focused in Fig. 10, and the ghosts are mapped back to the true target location leading to an increase in the SCR. However, there is a small remnant of the ghost w.r.t wall-3 in Fig. 11. For comparison, consider the ratio of the maxima at the target location to the maxima at all the ghosts locations. This ratio has a value of 0.98 for Fig. 9, whereas in Fig. 11, it is 2.5. There is a four fold reduction in the maxima due to the ghosts in Fig. 11. Although this artifact may still be considered as a false positive in the image in Fig. 11, it is highly unlikely that after using segmentation and detection algorithms (such as those presented in [24, 25]), it may still yield a false target in the final post detection (binarized) image. This remnant is attributed to the mapping of the multipath ghost w.r.t wall-2 when the imaged pixel is at the ghost location corresponding to the actual multipath w.r.t wall-3. In other words, there is an overlap of the actual multipath ghost and the hypothesized multipath ghost as explained in Fig. 8. In such scenarios, setting the variance equal to the systems range resolution is effective as seen in Fig. 10, since targets which are separated by less than the range resolution cannot be satisfactorily resolved. From our extensive simulations, we found that a lower variance must be chosen for smaller dimension rooms. For small rooms, it is logical to assume that the ghosts and higher order multipath are located quite close to one another. Therefore, it becomes prudent to be conservative

in selecting the variances. Large variances for smaller rooms lead to false mappings. Thus, variance selection for the problem at hand must be guided by the actual dimensions of the room.

An easier and simpler alternative to remove the remnant in Fig. 11 is to use a pre-processing mask as explained subsequently in multiple target scenarios. However, an improvement to the weighting functions can be envisioned when examining the spread of the target and ghosts. In our approach, we have considered that the 2D Gaussians weighting functions have a scaled identity covariance matrix. A natural improvement, albeit not pursued here, is to let the variance in the y-direction to be equal to the systems range resolution, the variance in the x-direction to be equal to the systems crossrange resolution, and introducing a correlation which is a function of the actual ghost location. This ensures that the ensuing weighting functions are rotated and sheared accordingly, nevertheless at a higher computational cost. As a tradeoff for satisfactory results vs. computational complexity, we choose the scaled identity covariance instead and defer the more complex approach to future work.

The simulations thus far have not considered system noise. We repeated the simulation in Fig. 9, considering a 5dB system signal-to-noise ratio (SNR) with the noise being zero mean, complex circular Gaussian distributed, added at each sensor independently. The noisy beamformed image is shown in Fig. 12(a), and the corresponding multipath exploited image is depicted in Fig. 12(b). Comparing Fig. 9 and Fig. 12(a), we observe that the noise has indeed distorted the image. However, comparing Fig. 10 and Fig. 12(a), the noise has no noticeable effect on the exploitation. In other words, Fig. 12(a) and Fig. 10 for all practical purposes are identical to one another.

Remnants, such as the one in Fig. 11, may not always appear, as seen from the next example. In Fig. 13(a), the target is at location (-12, 14). The associated multipath ghosts accompany the target and are seen in the figure. The intermediate image $I_1(\cdot)$ with a variance equal to the system

range resolution is seen in Fig. 13(b), which shows that most of the energy from the ghosts has been focused at the target location, as indicated by the presence of deep nulls at the ghost locations. The composite multipath exploited image is shown in Fig. 13(c). Although from row two in Table I, we see that the errors are large w.r.t wall-2, the results in the Fig. 13(c) show a well focused target, with no multipath ghosts, and an increase in the SCR at the original target location. An example of the destructive interference is provided in Fig. 13(d), wherein exploitation is carried out using (29). It is clear from this figure that there is a significant loss of SCR at the true target location, thereby causing the mapping to appear erroneous. Also, false targets are induced as a result of arbitrary regions where constructive interference occurs, and their locations do not coincide with the target locations or the original multipath ghost locations.

An example of the exploitation technique for a two-target scenario is shown in Fig. 14. We can clearly see from Fig. 14(a), that there are two targets at $(-4, 14)$ and $(-12, 12)$, and their associated multipath ghosts. The image after using (31-32) is shown in Fig. 14(b), we can see one of the remnants of the ghost w.r.t wall-1 and associated to the target at $(-12, 12)$. After careful analysis, we found out that a part of the ghost w.r.t wall-2 of the first target at $(-4, 14)$ is being mapped back to the ghost w.r.t wall-1 of the second target. This mapping is understood by examining Fig. 14(c), which shows the weighting when the imaged pixel is located at the ghost w.r.t wall-1 corresponding to the second target. A simple technique to get rid of the remnants is to use a pre-processing mask similar to the one in [12], the final image is then obtained as,

$$I_f(x_1, y_1) = I_{bin1}(x_1, y_1) \times I_1(x_1, y_1) \times |I(x_1, y_1)|$$

$$I_{bin1}(x_1, y_1) := \begin{cases} 1, & I_1(x_1, y_1) / \max_{\forall(x_1, y_1)} \{I_1(x_1, y_1)\} > \lambda_{th} \\ 0 & \text{otherwise} \end{cases} \quad (29)$$

where λ_{th} is a predefined threshold. Since detection strategies are not the focus of the paper, and noting that $I_1(x_1, y_1) / \max_{\forall(x_1, y_1)} \{I_1(x_1, y_1)\} \in [0, 1]$, a threshold set at $\lambda_{th} = 0.5$ proves effective.

Assuming noise plus clutter hypothesis, and target(s) only hypothesis, we can see that this threshold weights both these hypotheses in an equally likely fashion. Other sophisticated clustering schemes with number of clusters equal to two may also be used. After using the exploitation technique along with (29), we obtain Fig. 14(d) in which the remnant completely disappears. From our extensive analysis, such false peaks and remnants could be easily eliminated using the procedure given in (29). For the second target the respective LS errors are given in Table I. The first target location is identical to that in Fig. 9, and hence its corresponding LS errors are identical to those corresponding to this figure in Table I.

The last example shows that multiple targets are handled by the technique, but more importantly, demonstrates a scenario when the ghost locations may not share a one-to-one mapping with a particular target, which is further compounded by the system's point spread function. As a note, this problem maybe alleviated by using the correlated Gaussian weighting functions which are not pursued here but noting that a simple technique such as (29) suffices instead.

As noise was not added in many of the simulations and, thus, to be objective, we consider the signal SCR, defined as the ratio of the power in the target regions to the power in the rest of the image as the performance measure [17]. An example of the target region is shown in Fig. 15 for the original image corresponding to the two target scenario of Fig. 14(a). From Fig. 15, it is clear that we consider the ghosts to be in the clutter region. The SCRs before and after multipath exploitation (before (29)) are provided in Table II. It is readily seen that multipath exploitation has indeed increased the SCR even in scenarios where remnants were present after the procedure.

As far as the processing time associated with the proposed multipath exploitation technique is concerned, the computation time for generating Fig. 10 from Fig. 9 is about 4 hours on a

Workstation with 3.72 GHz Pentium Xeon processor and 4 GB of memory, running Matlab[®] ver. 2007a. In practice, the computations may be alleviated by performing the ghost focusing analysis offline.

To validate the technique experimentally, a through-the-wall SAR system was set up in the Radar Imaging Lab at Villanova University. A stepped-frequency signal with 696 steps covering 1-3GHz was used. The room dimensions are $D_1 = 5.09\text{m}$ and $D_2 = 3.78\text{m}$. The side walls and part of the floor were covered with absorbers and only multipath due to the back wall was considered. The front concrete wall is 0.15m thick with a dielectric constant of 7.66. The synthetic aperture consisted of an 81-element monostatic linear array with an inter-element spacing of 2.22cm. The standoff distance of the array from the front wall is 1.53m.

In the first experiment, a 0.35m diameter metal sphere was used as a target. The corresponding beamformed image is depicted in Fig. 16(a); both the target and the ghost are seen. The result after multipath exploitation is provided in Fig. 16(b). One can readily see that the ghost has been mapped back to the target. We also note that some of the other complex target-room interactions are left as is in the exploited image.

A second experiment was conducted with two targets, the first being the sphere used previously in the single target case, while the second was a smaller metallic sphere of 0.2032m diameter. The system parameters were identical to the single target case. The corresponding beamformed image is shown in Fig. 17(a), in which the targets as well as the ghosts with respect to the back wall are seen. The multipath exploited image is provided in Fig. 17(b), in which one can see that the ghosts have been mapped back to the target locations. We again observe that the other target-room and target-target interactions are retained in Fig. 17(b).

VI. CONCLUSIONS

A mathematically rigorous ray tracing approach was introduced to derive a multipath model. The model was derived considering reflections inside an enclosed room comprised of four walls. The walls were assumed to be homogenous, and smooth yielding specular reflections. Using the model, we illustrated the multipath ghosts in the beamformed image and showed that they were well focused. In particular, our analysis demonstrated that the multipath corresponding to each sensor appeared on the wall but changes position from one sensor to another. Hence, a least squares technique was derived to estimate its actual focusing location in both downrange and crossrange. The model was utilized to develop a multipath exploitation technique which associates multipath ghosts with their respective targets and maps them to their true target locations. This technique reduced the false positives in the original beamformed image as well as increased the SCR at the true target locations. Numerical simulations and experimental data were used to validate the findings.

APPENDIX-A

Derivations for time delays and angles for various paths

The one way time delays for the various paths in Fig. 2 can be derived from geometry, and are readily given as

$$\begin{aligned}
 \tau_A^{(n)} &= \left(d_1 \sqrt{\varepsilon_1} \sec(\psi_{rA}^n) + (y_t - d_1) \sec(\psi_{iA}^n) \right) / c \\
 \tau_B^{(n)} &= \left(d_1 \sqrt{\varepsilon_1} \sec(\psi_{rB}^n) + (y_{Bn} - d_1) \sec(\psi_{iB}^n) + x_t \operatorname{cosec}(\psi_{iB}^n) \right) / c \\
 \tau_C^{(n)} &= \left(d_1 (\sqrt{\varepsilon_1} \sec(\psi_{rC}^n) - \sec(\psi_{iC}^n)) + (2D_1 + 2D_y - y_t) \sec(\psi_{iC}^n) \right) / c \\
 \tau_D^{(n)} &= \left(d_1 \sqrt{\varepsilon_1} \sec(\psi_{rD}^n) + (y_{Dn} - d_1) \sec(\psi_{iD}^n) + (D_2 - x_t) \operatorname{cosec}(\psi_{iD}^n) \right) / c
 \end{aligned} \tag{30}$$

The expressions for the coordinates of B_n , C_n , and D_n are given by

$$\begin{aligned}
y_{Bn} &= y_t - x_t \cot(\psi_{iB}^n) \\
x_{Cn} &= x_t + (D_1 + D_y - y_t) \tan(\psi_{iC}^n) \\
y_{Dn} &= y_t - (D_2 - x_t) \cot(\psi_{iB}^n)
\end{aligned} \tag{31}$$

Equations (30-31) depend on the angles of incidence and refraction. Since the standoff distance is a known constant, then by projecting the various paths to the x-axis, we obtain the following equations which are useful in calculating the various angles.

$$\begin{aligned}
d_1 \tan(\psi_{rA}^n) + (y_t - d_1) \tan(\psi_{iA}^n) - D_{xn} + x_t &= 0 \\
d_1 \tan(\psi_{rB}^n) + (y_{Bn} - d_1) \tan(\psi_{iB}^n) - D_{xn} &= 0 \\
(2D_1 + 2D_y - y_t) \tan(\psi_{iC}^n) + d_1 (\tan(\psi_{rC}^n) - \tan(\psi_{iC}^n)) - D_{xn} + x_t &= 0 \\
d_1 \tan(\psi_{rD}^n) + (y_{Dn} - d_1) \tan(\psi_{iD}^n) - D_2 + D_{xn} &= 0
\end{aligned} \tag{32}$$

The angles of refraction can be determined from Snell's law and are given by,

$$\psi_{rp}^n = \sin^{-1} \left(\frac{\sin(\psi_{ip}^n)}{\sqrt{\epsilon_1}} \right), p \in \{A, B, C, D\} \tag{33}$$

Substituting the angles of refraction from (33) in (32), and using the expressions for y_{Bn} and y_{Dn} from (31), we obtain a set of equations that can be solved using numerical optimization for the angles of incidence. The angles of refraction can then be given straightforwardly using (33). Numerical techniques, such as the Newton's method, would suffice; however, we used the 'fsolve' in Matlab[®] to find the roots (zeros) of the equations. It is clear from Fig. 2 and (30) that the direct path and the multipath have different range and crossrange coordinates. From (31), the coordinates of the reflections at the back and side walls being sensor dependent implies that the multipath presents itself at different locations to the different sensors.

APPENDIX-B

Reflection and Transmission Coefficients (Parallel Polarization) for Lossless Medium

Let E_i be the incident field which for our convenience is assumed to be vertically polarized and is identical at all the sensor positions. Consider Path-A in Fig. 2; the wave propagates from the radar along this path to the target, i.e., the one-way path. From the expressions of the coefficients derived for waves impinging at an oblique angle on a dielectric slab [23], we have for the n -th sensor

$$E_{An} = T_{1n} T_{2n} E_i, \quad T_{1n} = \frac{2\sqrt{\epsilon_1} \cos(\psi_{iA}^n)}{\cos(\psi_{iA}^n) + \sqrt{\epsilon_1} \cos(\psi_{rA}^n)}, \quad T_{2n} = \frac{2 \cos(\psi_{rA}^n)}{\cos(\psi_{iA}^n) + \sqrt{\epsilon_1} \cos(\psi_{rA}^n)} \quad (34)$$

where E_{An} denotes the strength of the EM wave at the target when the wave is transmitted from the n -th sensor position. Similarly, for the other paths we obtain

$$E_{Bn} = T_{3n} T_{4n} \Gamma_{1n} E_i, \quad T_{3n} = \frac{2\sqrt{\epsilon_1} \cos(\psi_{iB}^n)}{\cos(\psi_{iB}^n) + \sqrt{\epsilon_1} \cos(\psi_{rB}^n)}, \quad T_{4n} = \frac{2 \cos(\psi_{rB}^n)}{\cos(\psi_{iB}^n) + \sqrt{\epsilon_1} \cos(\psi_{rB}^n)}, \quad (35)$$

$$\Gamma_{1n} = \frac{-\sin(\psi_{iB}^n) + \sqrt{\epsilon_1} \cos(\psi_{rB1}^n)}{\sin(\psi_{iB}^n) + \sqrt{\epsilon_1} \cos(\psi_{rB1}^n)}, \quad \psi_{rB1}^n = \sin^{-1} \left(\frac{\cos(\psi_{iB}^n)}{\sqrt{\epsilon_1}} \right)$$

$$E_{Cn} = T_{5n} T_{6n} \Gamma_{2n} E_i, \quad T_{5n} = \frac{2\sqrt{\epsilon_1} \cos(\psi_{iC}^n)}{\cos(\psi_{iC}^n) + \sqrt{\epsilon_1} \cos(\psi_{rC}^n)}, \quad T_{6n} = \frac{2 \cos(\psi_{rC}^n)}{\cos(\psi_{iC}^n) + \sqrt{\epsilon_1} \cos(\psi_{rC}^n)} \quad (36)$$

$$\Gamma_{2n} = \frac{-\cos(\psi_{iC}^n) + \sqrt{\epsilon_1} \cos(\psi_{rC}^n)}{\cos(\psi_{iC}^n) + \sqrt{\epsilon_1} \cos(\psi_{rC}^n)},$$

$$E_{Dn} = T_{7n} T_{8n} \Gamma_{3n} E_i, \quad T_{7n} = \frac{2\sqrt{\epsilon_1} \cos(\psi_{iD}^n)}{\cos(\psi_{iD}^n) + \sqrt{\epsilon_1} \cos(\psi_{rD}^n)}, \quad T_{8n} = \frac{2 \cos(\psi_{rD}^n)}{\cos(\psi_{iD}^n) + \sqrt{\epsilon_1} \cos(\psi_{rD}^n)}, \quad (37)$$

$$\Gamma_{3n} = \frac{-\sin(\psi_{iD}^n) + \sqrt{\epsilon_1} \cos(\psi_{rD1}^n)}{\sin(\psi_{iD}^n) + \sqrt{\epsilon_1} \cos(\psi_{rD1}^n)}, \quad \psi_{rD1}^n = \sin^{-1} \left(\frac{\cos(\psi_{iD}^n)}{\sqrt{\epsilon_1}} \right)$$

The one-way amplitudes associated with the transmission and reflection coefficients for the paths-A, B, C, and D are defined as,

$$T_{pn} = \frac{E_{pn}}{E_i}, \quad p \in \{A, B, C, D\} \quad (38)$$

ACKNOWLEDGMENT

The authors would like to acknowledge Dr. Wenji Zhang for performing the FDTD simulations, Dr. Graeme Smith for his valuable inputs to the derivation of the multipath ghost locations, and Dr. Giovanni Alli for the fruitful discussions regarding multipath exploitation for through-the-wall imaging applications

REFERENCES

- [1] E. J. Baranoski, "Through-wall imaging: historical perspectives and future directions," *Journ. of the Franklin Inst.*, vol. 345, no. 6, pp. 556-569, Sept. 2008.
- [2] L. M. Frazier, "Surveillance through walls and other opaque materials," *IEEE Aerosp. Electron. Systems Mag.*, vol. 11, no. 11, pp. 6-9, Oct. 1996.
- [3] D. D. Ferris Jr., N. C. Currie, "A survey of current technologies for through-the-wall surveillance (TWS)," in *Proc. SPIE conf. C3I Information, and Training Tech. for Law enforcement*, vol. 3577, pp. 62-72, Boston, MA, Jan. 1999.
- [4] E. F. Greneker III, "RADAR flashlight for through-the-wall detection of humans," in *Proc. SPIE conf. Targets & Backgrounds: Charact. & Representation IV*, vol. 3577, pp. 280-285, July 1998.
- [5] M. G. Amin (Ed.), *Through-the-wall radar imaging*, CRC press, New York, NY, Dec. 2010.
- [6] R. Linnehan, and J. Schindler, "Multistatic scattering from moving targets in multipath environments," in *Proc. IEEE Inter. Radar Conf.*, Pasadena, CA, 4-8 May 2009.
- [7] B. Chakraborty, Y. Li, J. J. Zhang, T. Trueblood, A. Papandreou-Suppappola, and D. Morell, "Multipath exploitation with adaptive waveform design for tracking in urban terrain," in *Proc. IEEE Inter. Conf. Acoust., Speech, and Signal process.*, Dallas, TX, 14-19 March 2010.

- [8] S. Sen, M. Hurtado, and A. Nehorai, "Adaptive OFDM radar for detecting a moving target in urban scenarios," in *Proc. Inter. Waveform Diversity and Design Conf.*, Orlando, FL, 8-13 Feb. 2009.
- [9] J. L. Krolik, J. Farell, and A. Steinhardt, "Exploiting multipath propagation for GMTI in urban environments," in *Proc. IEEE Radar Conf.*, Verona, NY, 24-27 Apr. 2006.
- [10] F. Ahmad, "Multi-location wideband through-the-wall imaging," in *Proc. IEEE Inter. Conf. Acoust. Speech, and Sig. Processing*, pp. 5193-5196, Las Vegas, NV, 2008.
- [11] R. J. Burkholder, "Electromagnetic models for exploiting multi-path propagation in through-wall radar imaging," in *Proc. Inter. Conf. on Electrmag. in Adv. Appl.*, pp. 572-575, Torino, Italy, Sep 2008.
- [12] T. Dogaru and C. Le, "SAR images of rooms and buildings based on FDTD computer models," *IEEE Trans. Geosci. and Remote Sensing*, vol. 47, no. 5, pp. 1388-1401, 2008.
- [13] S. Kidera, T. Sakamoto, and T. Sato, "Experimental study of shadow region imaging algorithm with multiple scattered waves for UWB radars," *PIERS Online*, vol. 5, no. 4, pp. 393-296, 2009.
- [14] P. Setlur, M. Amin, and F. Ahmad, "Multipath Doppler signatures from targets moving behind walls," in *Proc. IEEE Inter. Radar Conf.*, Washington D. C., 10-14 May 2010.
- [15] P. Setlur, F. Ahmad, G. E. Smith, and M. Amin, "Multipath analyses of moving targets in enclosed structures using Doppler radars," in *Proc. SPIE conf. Radar Sensor Tech. XIV*, Orlando, FL, 2010.
- [16] P. Setlur, *Statistical Algorithms and Bounds for Moving Targets in Urban Sensing and Through-the-Wall Radar Applications*, PhD Thesis, Villanova University, May 2010.

- [17] Y.-S. Yoon, and M. Amin, "Spatial filtering for wall-clutter mitigation in through-the-wall radar imaging," *IEEE Tran. Geosci. Remote Sensing*, vol. 47, no. 9, pp. 3192-3208, Aug. 2009.
- [18] M. Dehmollaian, and K. Sarabandi, "Refocusing through building walls using synthetic aperture radar," *IEEE Tran. Geosci. Remote Sensing*, vol. 46, no. 6, pp. 1589-1599, Jun. 2008.
- [19] F. Ahmad, M. Amin, and S. A. Kassam, "Synthetic aperture beamformer for imaging through a dielectric wall," *IEEE Trans. Aerospace and Electron. Sys.*, vol. 41, no. 1, pp. 271-283, Jan. 2005.
- [20] Y. Yang, C. Zhang, and A. E. Fathy, "Development and implementation of ultra-wideband see-through-wall imaging system based on sampling oscilloscope," *IEEE Ant. and Prop. Lett.*, vol. 7, pp. 465-468, Dec. 2008.
- [21] F. Ahmad, Y. Zhang, and M. Amin, "Three-dimensional wideband beamforming for imaging through a single Wall," *IEEE Geosci. Remote Sensing Lett.*, vol. 5, no. 2, pp. 176-179, 2008.
- [22] G. Wang, M. Amin, and Y. Zhang, "A new approach for target locations in the presence of wall ambiguity," *IEEE Trans. Aerospace and Electron. Sys.*, vol. 42, no. 1, pp. 301-315, 2006.
- [23] C. A. Balanis, *Advanced Engineering Electromagnetics*, John Wiley, New York, Apr. 2009.
- [24] C. Debes, J. Hahn, A. M. Zoubir, and M. G. Amin, "Feature extraction in through-the-wall radar imaging," *In Proc. IEEE Inter. Conf. Acoust., Speech, and Signal process.*, Dallas, TX, March 2010.
- [25] A. Martone, K. Ranney, and R. Innocenti, "Automatic through the wall detection of moving targets using low-frequency ultra-wideband radar," in *Proc. IEEE Inter. Radar Conf.*, Washington, DC, 2010.

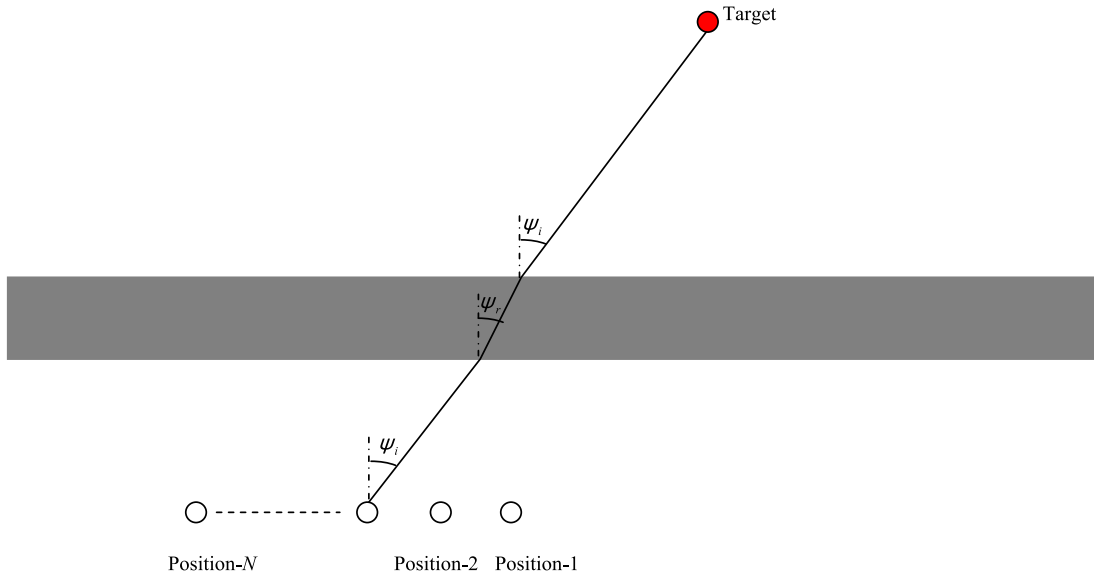


Fig. 1. TTW SAR model.

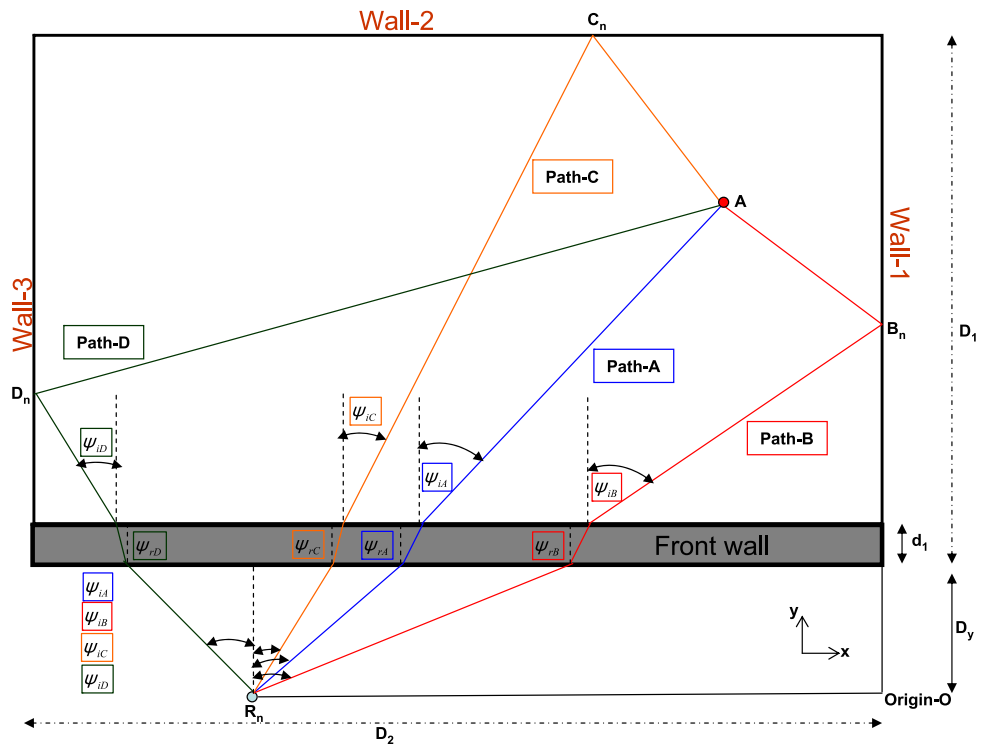


Fig. 2. Multipath model.

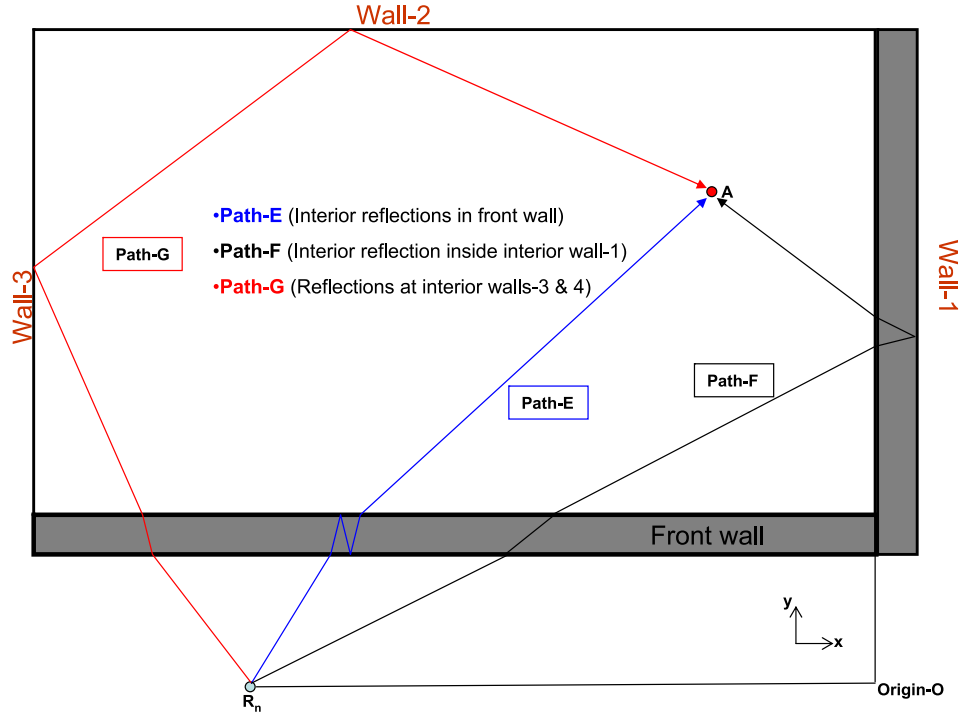


Fig. 3. Other higher order paths.

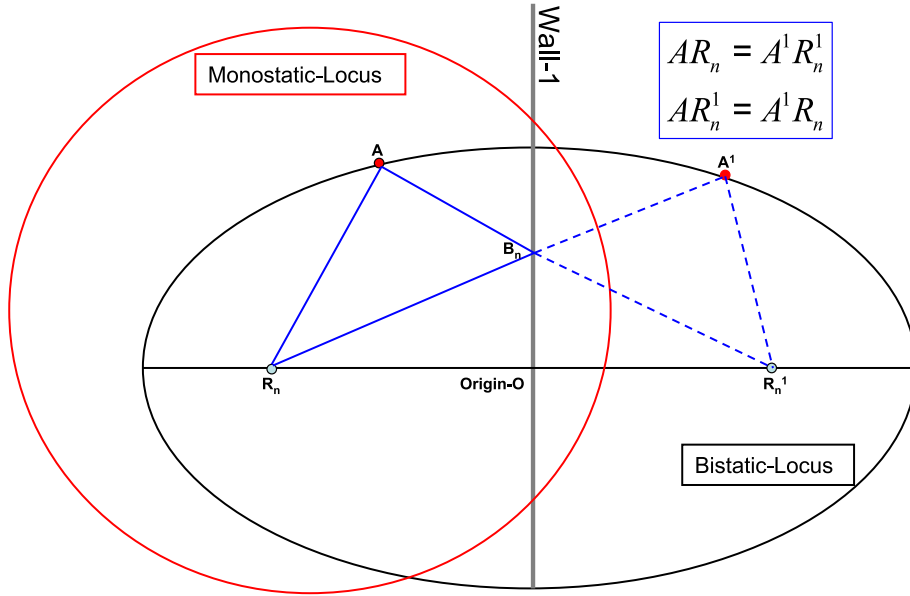


Fig. 4. The equivalence between the bistatic and monostatic geometries.

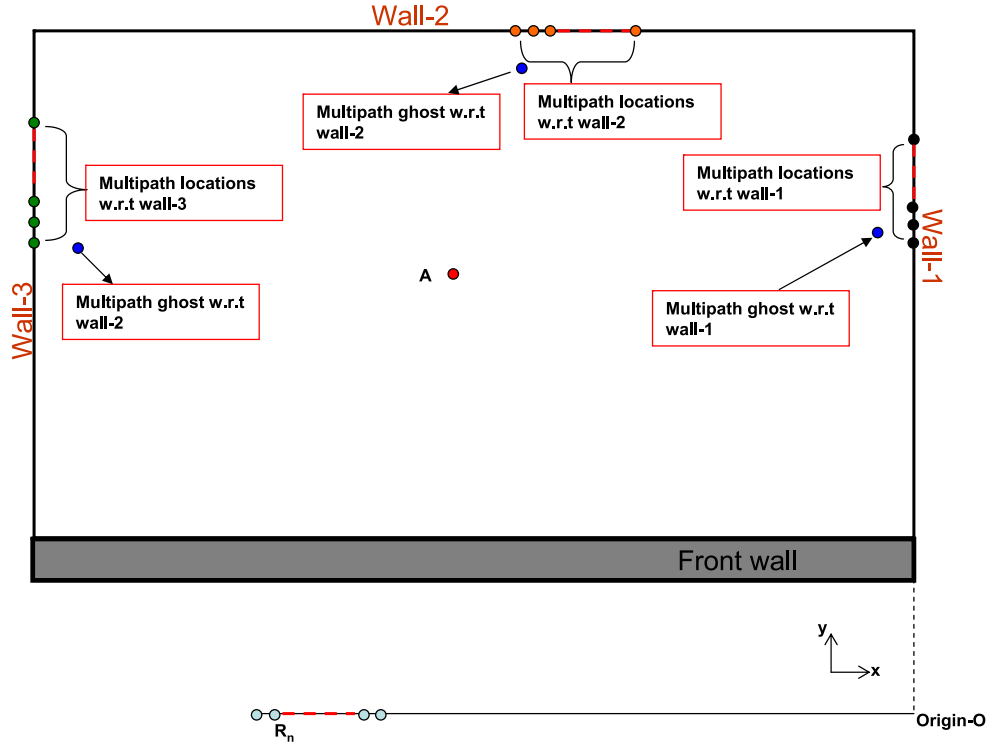


Fig. 5. Multipath locations and final location of multipath ghosts.

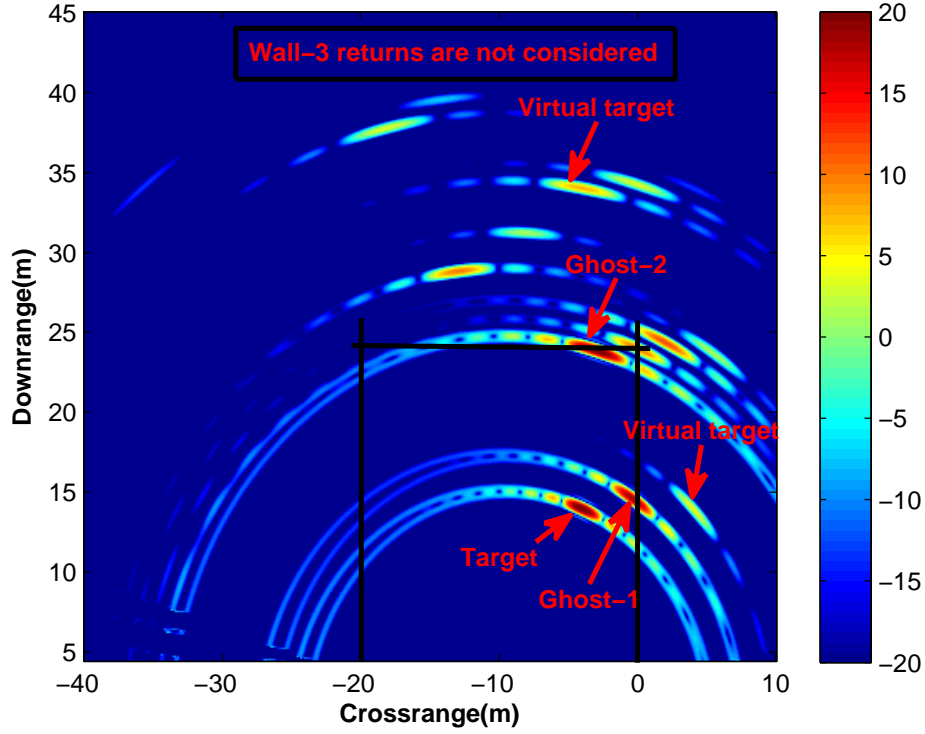


Fig. 6. Beamformed image with ghosts w.r.t to all wall-1 and wall-2 and other higher order paths.

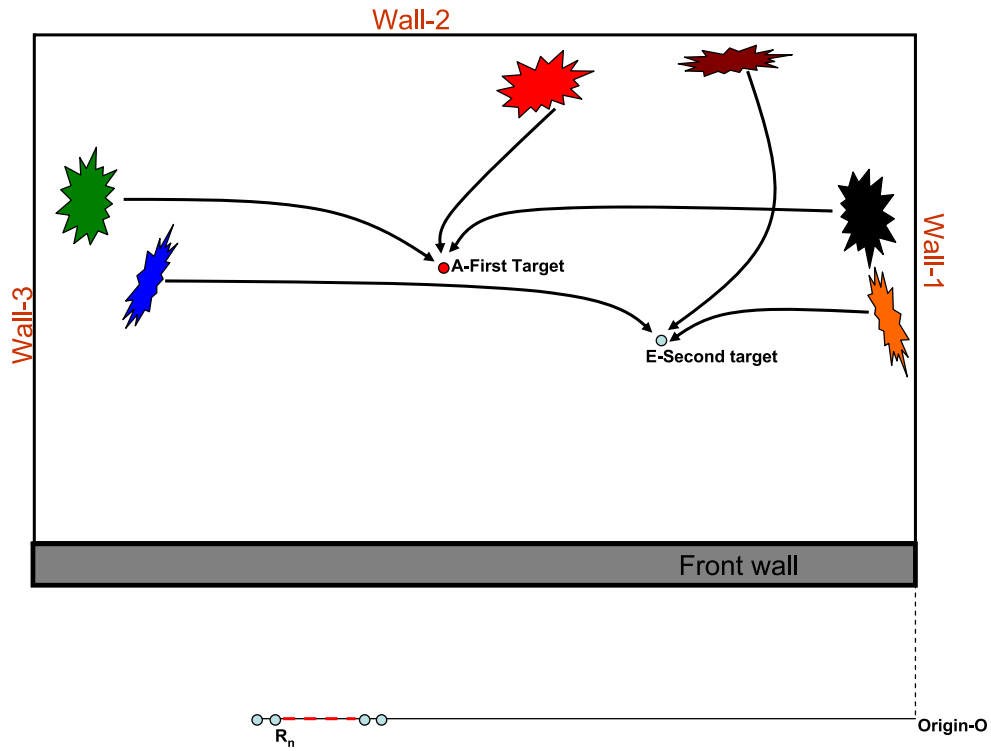


Fig. 7. Multipath exploitation principle.

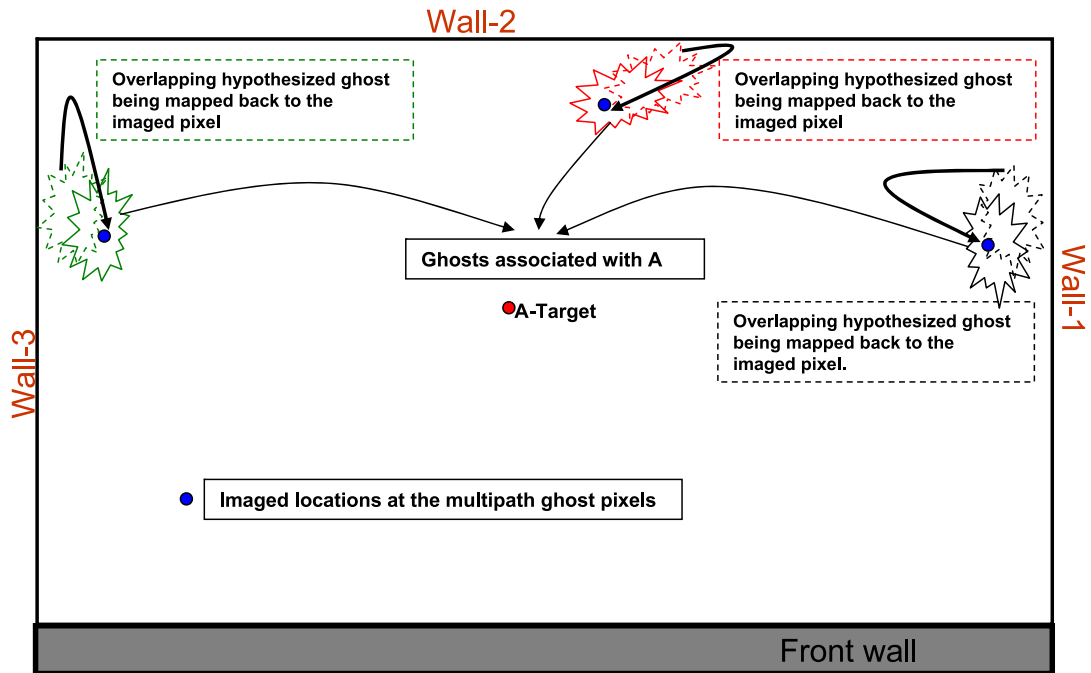


Fig. 8. Significance of second weighting function.

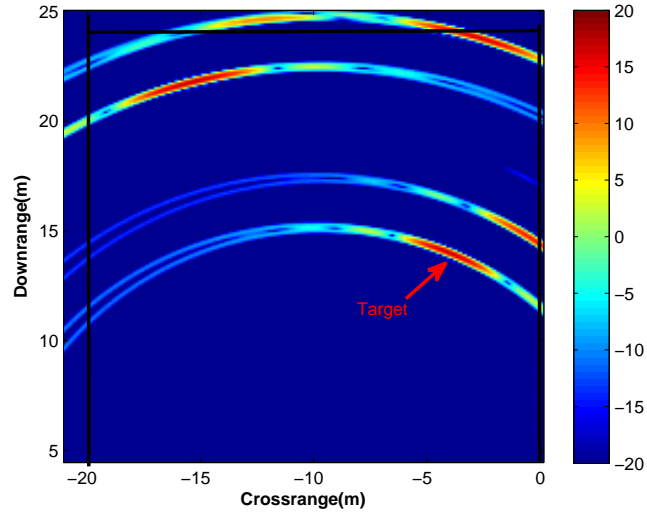


Fig. 9. Beamformed image of target close to wall-1, along with respective ghosts.

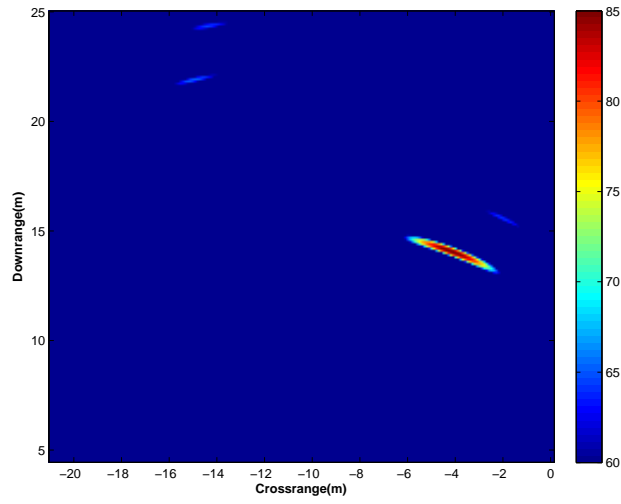


Fig. 10. Exploitation with variance equal to system range resolution.

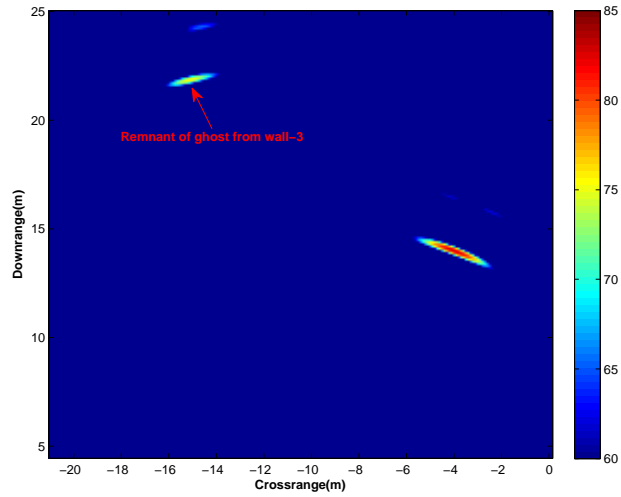


Fig. 11. Exploitation with variance equal to system wavelength.

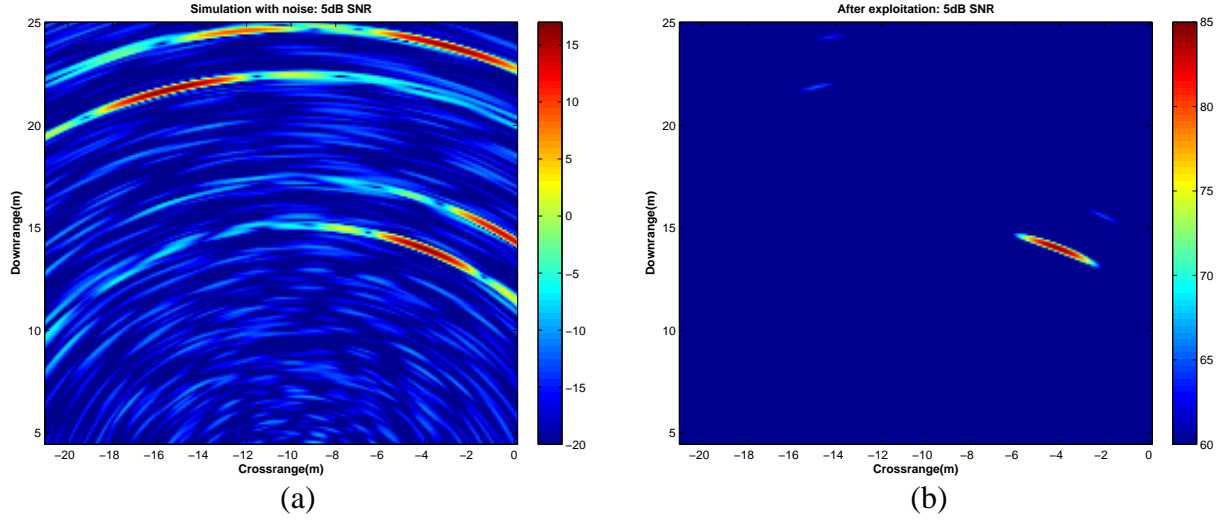


Fig. 12. Noisy example, (a)original in 5dB SNR, (b)after exploitation with variance set at system range resolution.

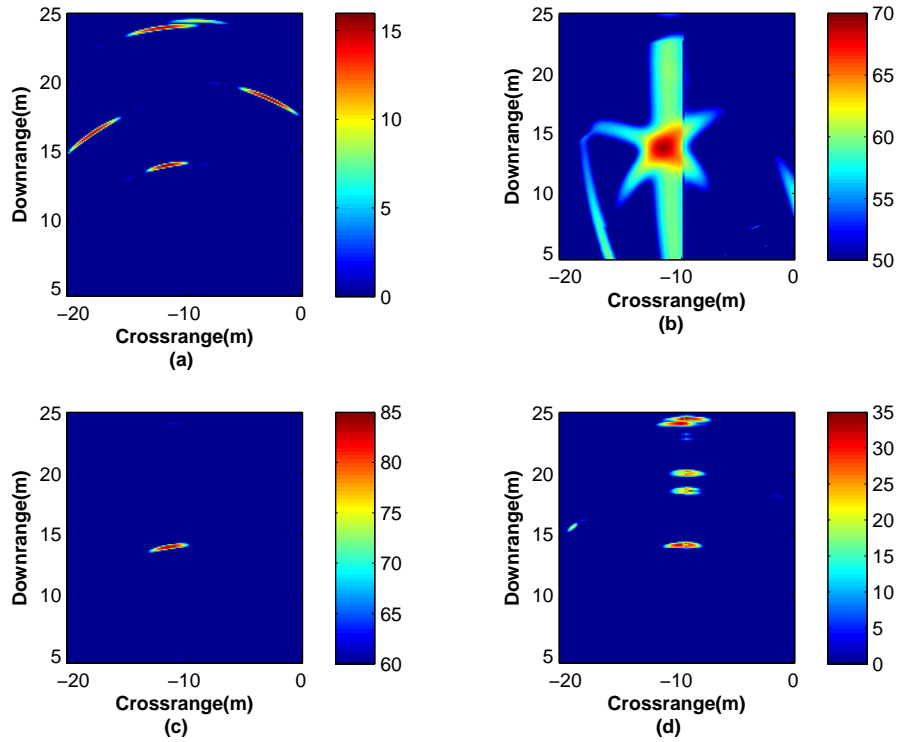


Fig. 13. For a target close to wall-3, (a) original beamformed image, (b) intermediate image, (c) after exploitation, and (d) example of destructive interference.

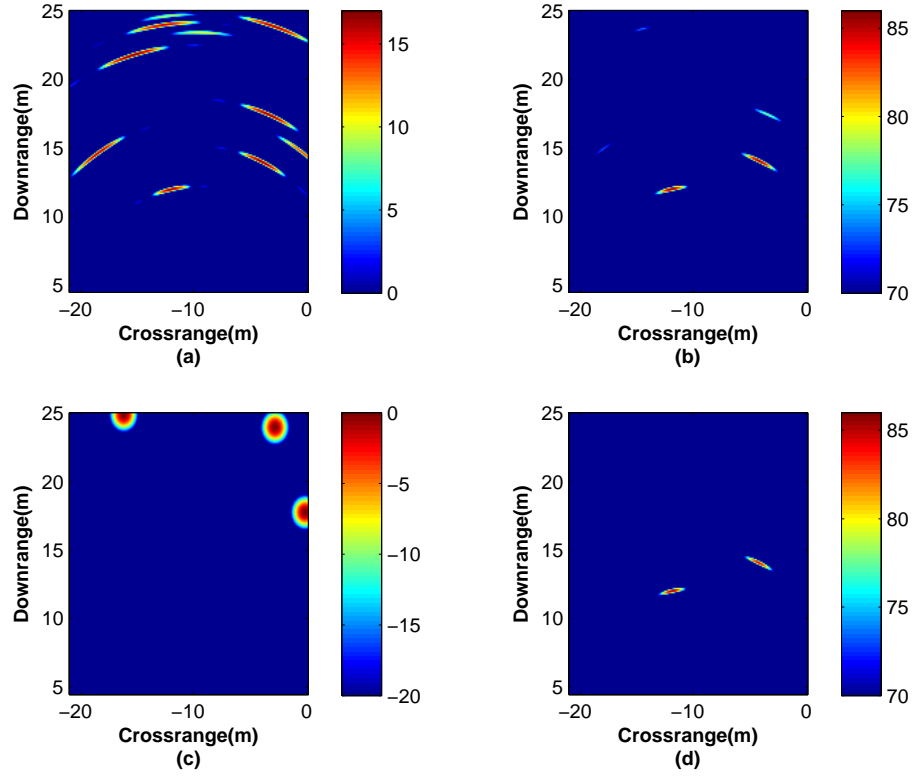


Fig. 14 Multiple target scenario, (a) original beamformed image, (b) after multipath exploitation with equation (27-28), (c) weighting functions at ghost location $(-3.3, 17.4)$ w.r.t wall-2 associated with second target $(-12, -12)$, and (d) exploitation technique with equation (29).

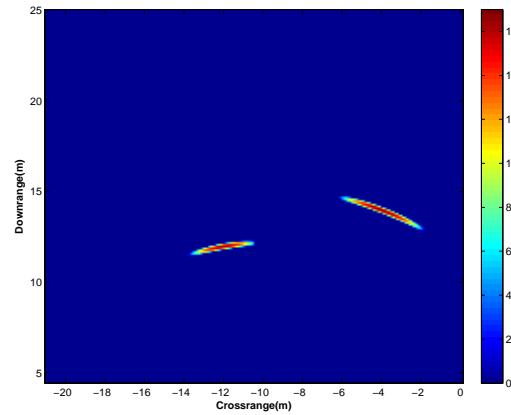


Fig. 15 Target region definition in the SCR. Target region here corresponds to the target locations as in Fig. 13(a) without the associated ghosts.

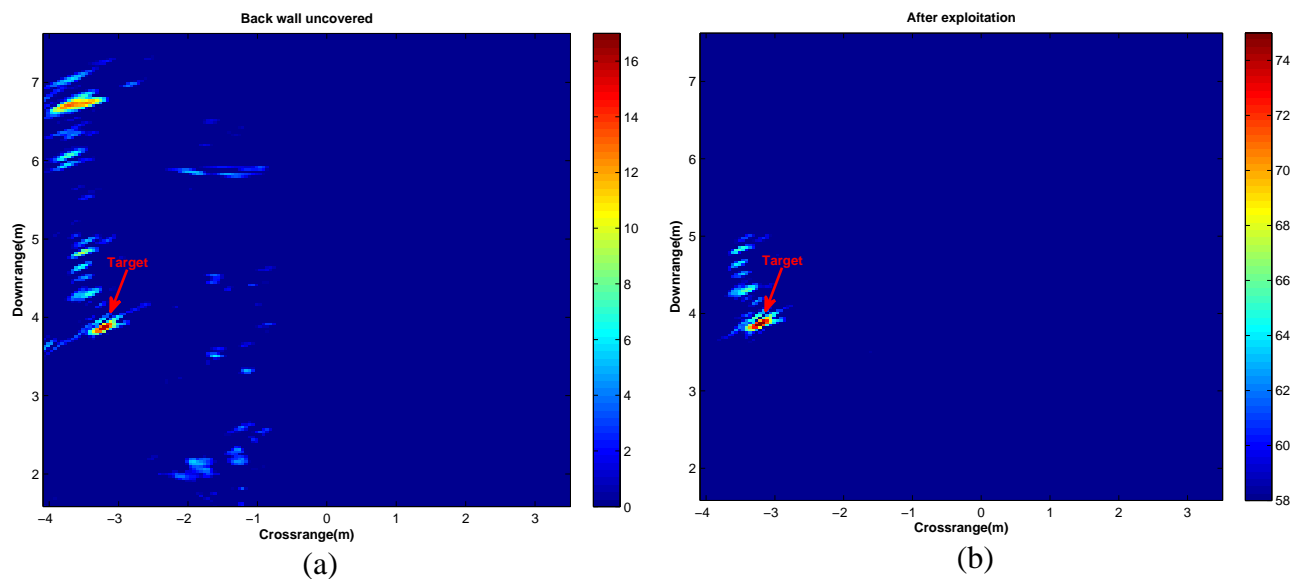


Fig. 16 Single target experiment: (a) Original, (b) after multipath exploitation.

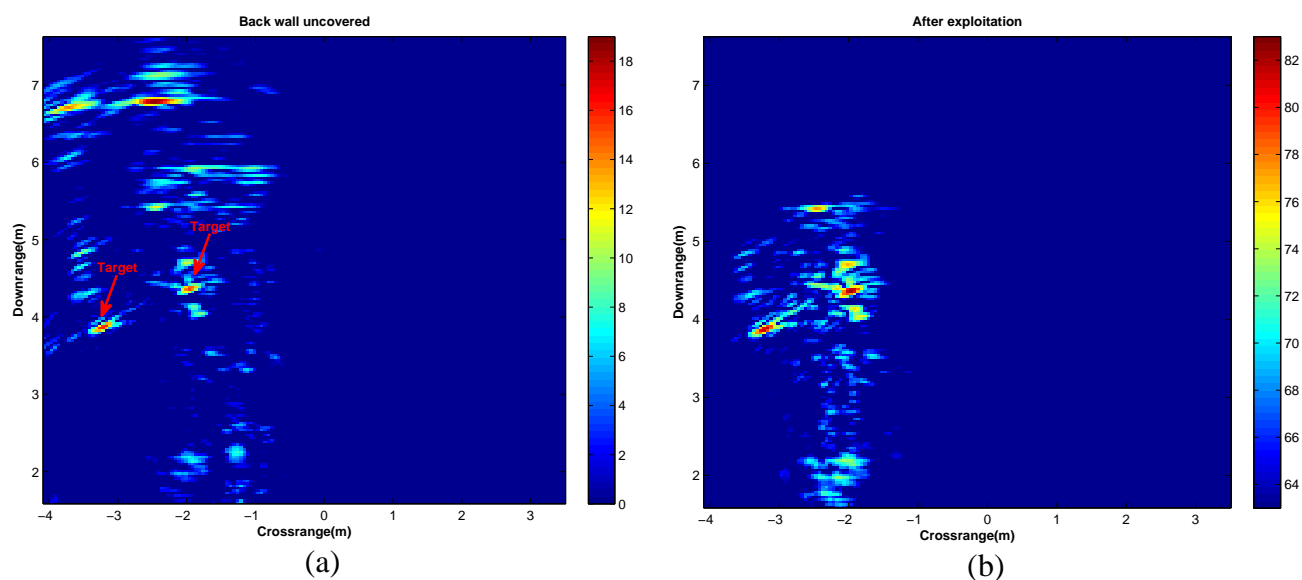


Fig. 17 Two target experiment: (a) Original , (b) after multipath exploitation.

Table. I Errors in estimates (after appropriate rounding w.r.t the sampling in range and crossrange) of the multipath ghost locations as predicted by LS.

	Errors: Wall-1 (downrange, crossrange)	Errors: Wall-2 (downrange, crossrange)	Errors: Wall-3 (downrange, crossrange)
Fig. 9	(0.0,0.0)	(0.1,0)	(0.6, 0.3)
Fig. 13(a)	(0.1, 0.2)	(0.7,0.5)	(0, 0.1)
Fig. 14(a) (Second target)	(0.3, 0.2)	(0.6, 0.5)	(0.3, 0.1)

Table. II SCR(in dBs) before and after multipath exploitation for the simulations.

SCR (dB)	Fig.9	Fig. 13(a)	Fig. 14(a)
Before	-5.98	-6.85	-6.68
After	14.83	18.22	6.51